Electrochimica Acta 184 (2015) 452–465

Contents lists available at ScienceDirect

Electrochimica Acta

journal homepage: www.elsevier.com/locate/electacta

Optimal Electrocatalytic Pd/MWNTs Nanocatalysts toward Formic Acid Oxidation

Yiran Wang[a], Qingliang He[a], Huige Wei[b], Jiang Guo[a], Keqiang Ding[c], Qiang Wang[d], Zhe Wang[e], Suying Wei[b,*], Zhanhu Guo[a,*]

[a] Integrated Composites Laboratory (ICL), Department of Chemical & Biomolecular Engineering, University of Tennessee, Knoxville, TN 37996 USA
[b] Department of Chemistry and Biochemistry, and Dan F. Smith Department of Chemical Engineering, Lamar University, Beaumont, TX 77710 USA
[c] College of Chemistry and Materials Science, Hebei Normal University, Shijiazhuang, Hebei 050024 China
[d] College of Environmental Science and Engineering, Beijing Forestry University, Beijing 100083 China
[e] Chemistry Department, Xavier University, New Orleans, LA 70125 USA

ARTICLE INFO

Article history:
Received 18 June 2015
Received in revised form 8 October 2015
Accepted 9 October 2015
Available online 22 October 2015

Keywords:
formic acid oxidation
dual pathway
palladium based catalysts
concentration effect
temperature effect

ABSTRACT

The operating conditions such as composition of electrolyte and temperature can greatly influence the formic acid (HCOOH) oxidation reaction (FAOR). Palladium decorated multi-walled carbon nanotubes (Pd/MWNTs) were successfully synthesized and employed as nanocatalysts to explore the effects of formic acid, sulfuric acid (H_2SO_4) concentration and temperature on FAOR. Both the hydrogen adsorption in low potential range and the oxidation of poisoning species during the high potential range in cyclic voltammetry were demonstrated to contribute to the enhanced electroactivity of Pd/MWNTs. The as-synthesized Pd/MWNTs gave the best performance under a condition with balanced adsorptions of HCOOH and H_2SO_4 molecules. The dominant dehydrogenation pathway on Pd/MWNTs can be largely depressed by the increased dehydration pathway, leading to an increased charge transfer resistance (R_{ct}). Increasing HCOOH concentration could directly increase the dehydration process proportion and cause the production of CO_{ads} species. H_2SO_4 as donor of H^+ greatly facilitated the onset oxidation of HCOOH in the beginning process but it largely depressed the HCOOH oxidation with excess amount of H^+. Enhanced ion mobility with increasing the temperature was mainly responsible for the increased current densities, improved tolerance stabilities and reduced R_{ct} values, while dehydration process was also increased simultaneously.

1. Introduction

Dramatic attentions have been paid to direct liquid fuel cells such as direct alcohol fuel cells (DAFCs) and direct formic acid fuel cells (DFAFCs) due to their promising applications in energy-related devices [1–3] and scientific attracting merits such as high energy conversion efficiency, low environmental pollution, and low operating temperature [4,5]. For DFAFCs, renewable formic acid (FA) as a potential micro-power liquid fuel owes high theoretical open circuit potential (1.45 V) and is environmental-friendly when dissolved in water [6–8]. Less effects of crossover through the proton exchange membrane and easy oxidization at less positive potential with faster kinetics are also obtained comparing with that of methanol [9–11]. Therefore, FA as an alternative fuel choice has become increasingly competitive due to its potential advantages compared with other fuels.

In order to reach wide commercialization of fuel cells, highly active electrocatalysts with acceptable low price are continuing pursued in anode materials for fuel oxidation and in cathode for oxygen reduction [12]. Platinum (Pt), well known for its excellent catalytic activity for electrooxidation of methanol, exhibits less satisfactory performance for FA oxidation, the surface of Pt is easily poisoned by the strong adsorbed CO_{ads} species produced during the oxidation of FA to have a further lowered catalytic performance [13–15]. Furthermore, the high cost and limited world supply also motivate extensive researches to the development of non-Pt catalysts [16,17]. Palladium (Pd) with similar properties to Pt (same group in the periodic table, same fcc crystal structure, similar atomic size) and certain advantages compared to Pt (lower price, greater resistance to CO, and inherently faster kinetics in alkaline

* Corresponding authors.
E-mail addresses: suying.wei@lamar.edu (S. Wei), zguo10@utk.edu (Z. Guo).

http://dx.doi.org/10.1016/j.electacta.2015.10.046
0013-4686/

medium) is emerging as a suitable substitute for Pt in fuel cells [18–20]. In order to make full usage of Pd atoms, substrates are usually introduced to facilitate the dispersion of Pd nanoparticles (NPs) and to endow new properties to the final nanocomposites without causing any "pollutants" [21–24]. Carbon nanotubes (CNTs) have emerged as a promising candidate due to their excellent electronic properties, good physicochemical stability, and large specific surface area [25,26]. In addition, some oxygen containing groups are also introduced on the tube wall surface in order to facilitate the dispersion and deposition of the specific active materials [27,28].

Simple dual pathways are well-recognized for the decomposition of FA, i.e. dehydrogenation and dehydration pathways. The former may proceed via $HCOOH \rightarrow CO_2 + H_2$ or $HCOOH \rightarrow CO_2 + 2H^+ + 2e^-$ and the latter via $HCOOH \rightarrow CO_{ad} + H_2O$ [29,30]. The adsorbed CO species on electrode largely blocked the oxidation of fresh HCOOH molecules and could be only oxidized at higher oxidation potentials [31]. Whether dehydrogenation or dehydration pathway is predominated mainly depending on the nature of catalyst or the electrode potential, the dehydrogenation pathway is definitely highly desired in designing new catalysts for its better utilization of chemical energy stored in FA [32]. However, the raised amount of HCOOH produces increased poisoning species which conversely depress the dehydrogenation pathway and increase the dehydration pathway proportion [33].

FAOR primarily depends on the electrodes, electrolytes and operating conditions. Nowadays, numerous studies are focusing on the effects of structure and composition of the electrode materials, as well as the type of electrolyte on FAOR [34–37]. However, the practical operating conditions such as the electrolyte concentration and temperature are also important for the improvement of catalytic efficiency. Since the carbon supported Pd catalysts usually exhibit a well-defined performance for FAOR in acidic electrolyte [38–40]. Sulfuric acid (H_2SO_4) as a strong acid is widely employed to facilitate both electronic and proton transports within the anode compartment of DFAFCs [41]. A proper combination of H_2SO_4 and HCOOH concentrations would probably contribute to the highest electro-activity of the corresponding catalysts due to the provided favorable environment. In addition, temperature as an inevitable factor should also be taken into account since different regions on the earth experience distinct climate conditions. For example, the temperature of frigid winter in some European countries is always below 0 °C while some Asia and Africa regions need to go through the ablaze of the summer that may reach up 40 °C. Since the performances of catalysts toward FAOR reported nowadays are mostly focused on the room temperature which is not applicable in the above-mentioned extreme environment conditions, a study of the temperature effect on FAOR is of great significance in consideration of practical applications.

In this work, the as-synthesized Pd decorated multi-walled carbon nanotubes (Pd/MWNTs) were used as nanocatalysts to investigate the electrolyte concentration and temperature effects on FAOR. The catalytic performances in different combinations of HCOOH and H_2SO_4 concentrations were investigated to explore the variation of dual pathway of FAOR and to probe the optimal combination of HCOOH and H_2SO_4 concentrations. Three temperatures, i.e., 2, 22, and 40 °C represent cold, normal and hot weather were selected to investigate the temperature effects on FAOR. The electrochemical characterizations such as cyclic voltammetry (CV) with different scan ranges, chronoamperometry (CA) with different set-voltages, electrochemical impedance spectroscopy (EIS) at various potentials and slow linear sweep voltammetry (SLV) were employed to comprehensively characterize the oxidation process and poisoning effect. The inherent dual pathway process of FAOR was also proposed based on the above experimental results.

2. Experimental

2.1. Materials and Nanocatalysts Preparation

Solvent xylene (laboratory grade, $\rho = 0.87\ g/cm^3$), sulfuric acid (H_2SO_4, 95.0%–98.0%) and formic acid (HCOOH, reagent grade, ≥95%) were purchased from Fisher Scientific. Palladium (II) acetylacetonate ($Pd(C_5H_7O_2)_2$, 99%, Mw = 304.64 g/mol) and ethanol (anhydrous, C_2H_5OH, ≥99.5%) were purchased from Sigma Aldrich. Acetone (CH_3COCH_3, ACS Grade, assay ≥99.5%) was purchased from VWR International. Carboxylic group functionalized multi-walled nanotubes (MWNTs-COOH) (Stock**#:** 1272YJF, 95% purity, content of —COOH: 0.47–0.51 wt%, 50–80 nm diameter, 10–20 μm length) were provided by Nanostructured & Amorphous Materials, Inc. All the chemicals were used as-received without any further treatments.

The Pd/MWNTs nanocatalysts were synthesized using a method reported previously [42]. Briefly, 100.0 mg MWNTs-COOH were dispersed in 60 mL xylene in a 100-mL beaker under sonication for one hour. It was transferred to a 250-mL 3-neck flask and heated to reflux (~140 °C) in ~20 min. 0.304 g palladium (II) acetylacetonate ($Pd(acac)_2$) with a well sonicated dispersion in 20 mL xylene was added to the refluxing MWNTs-COOH/xylene solution. The whole solution was refluxed continuously for additional 3 hours to complete the reaction. Finally, the solution was cooled down to room temperature naturally, filtered under vacuum and rinsed with ethanol and acetone 3 times, respectively.

2.2. Preparation of Pd/MWNTs working electrode

Prior to each experiment, the working glassy carbon electrode with a diameter of 3 mm was successively polished with 1 and 0.05 μm alumina powders on a microcloth wetted with DI water to provide an electrode with a mirror-like surface. For the preparation of a catalyst coated electrode, 1.0 mg catalyst was added to 1.0 mL ethanol solution of Nafion (the content of Nafion is 0.1 wt %), then the mixture was treated for 30 min with ultrasonication to form a uniform suspension. The obtained suspension (5 μL) was dropped on the surface of the well-treated glassy carbon electrode. Finally, the resultant modified glassy carbon electrode was dried naturally at room temperature.

2.3. Characterizations

X-ray diffraction (XRD) analysis of the nanocatalysts was carried out on a Bruker D8 ADVANCE X-ray diffractometer equipped with a Cu Kα source (λ = 0.154 nm) at 40 kV and 30 mA. The 2θ angular region between 20 and 70° was explored at a scan rate of $1^\circ\ min^{-1}$. A transmission electron microscope (TEM, JEOL 2010F) was used to characterize the morphology of the as-prepared nanocatalysts at a working voltage of 200 kV. The samples were prepared by drying a drop of ethanol suspension on a 400-mesh carbon-coated copper grid (Electron Microscopy Sciences). Raman spectra were obtained using a Horiba Jobin-Yvon LabRam Raman confocal microscope with 785 nm laser excitation at a $1.5\ cm^{-1}$ resolution at room temperature. X-ray photoelectron spectroscopy (XPS) measurements were performed on a Kratos AXIS 165 XPS/AES instrument. The samples were scanned with a monochromatic Al X-ray source at the anode of 10 kV and beam current of 15 mA. The Pd peaks were deconvoluted into the components on a Shirley background. Thermogravimetric analysis (TGA) was conducted using a TA instruments Q-500 at a heating rate of $10\ ^\circ C\ min^{-1}$ and an air flow rate of $60\ mL\ min^{-1}$ from 30 to 700 °C.

The electrochemical experiments were conducted in a conventional three-electrode cell. The as-prepared glassy carbon

electrode deposited with catalyst was used as the working electrode, platinum wire was employed as the counter electrode, and saturated calomel electrode (SCE) (0.241 V vs. SHE) connected to the cell through a Luggin capillary serving as the reference electrode. All the potentials were referred to the SCE. All the electrochemical measurements were performed on an electrochemical working station VersaSTAT4 potentiostat (Princeton Applied Research). Cycle voltammogram (CV) curves were recorded after sweeping potential cycles in specific potential region until CV curve was stable. The chronoamperometry (CA) was performed at 0, 0.2, 0.4 and 0.6 V for FAOR each for a duration of 300 s, respectively. The electrochemical impedance spectroscopy (EIS) was carried out in the frequency range from 100 000 to 0.1 Hz with a 5 mV amplitude at various potentials (vs. SCE, from −0.2 to 0.9 V) for FAOR. Slow linear sweep voltammetry (SLV) was measured from −0.8 to 0.2 V with a scan rate of 1.0 mV s^{-1} and the current density was normalized to the area of coated nanocatalysts.

3. Results and discussion

3.1. XRD, Raman, XPS, and TGA analysis

In order to characterize the crystalline structure, thermal property and the inner relationship between Pd NPs and MWNTs of the synthesized Pd/MWNTs, Common techniques such as XRD, Raman spectra, XPS and TGA are performed and shown in Fig. 1 (A–D) compared with the as-received MWNTs. For the XRD patterns, Fig. 1(A), pure MWNTs only exhibit one peak, belonging to C (0 0 2), however, three peaks belonging to Pd (1 1 1), Pd (2 0 0) and Pd (2 2 0) are clearly seen in Pd/MWNTs as confirmed from the standard Pd card (JCPDS # 05-0681) at the bottom, indicating the successful deposition of Pd on the tube wall surface [43]. For the Raman spectra, Fig. 1(B), both pure MWNTs and Pd/MWNTs exhibit similar D and G bands, arising from the defect sites and sp^2 hybridization of carbon materials [44]. In addition, in contrast to the perfect honeycomb lattice of graphite, the G band is splited into the G^- and G^+ bands due to the curvature of the CNTs [45]. The intensity ratio of D to G bands (I_D/I_G) provides information about the degree of structural defects on the tube wall. Specifically, the higher the ratio, the larger the degree of defects. An increased I_D/I_G value is calculated for Pd/MWNTs (1.85) vs. pure MWNTs (1.52), suggesting an interaction between Pd NPs and MWNTs due to the functionalized carboxyl groups and further confirming the successful deposition of Pd NPs [46]. The relationship between Pd NPs and MWNTs is also confirmed by the curve fitting of C 1s in XPS (Fig. 1(C)). The obvious area decreases of deconvoluted oxygen containing groups are clearly noticed after the deposition of Pd NPs on MWNTS due to the occupation of defects. Finally, the thermal stability of Pd/MWNTs and Pd loading is determined by TGA conducted in air atmosphere, Fig. 1(D). A slight weight decrease around 200 °C is due to the continue decomposing of acac and the following weight up is attributed to the oxidation of Pd. The Pd loading is obtained from the final residue (PdO) as 41.13 % after the total burn of MWNTs.

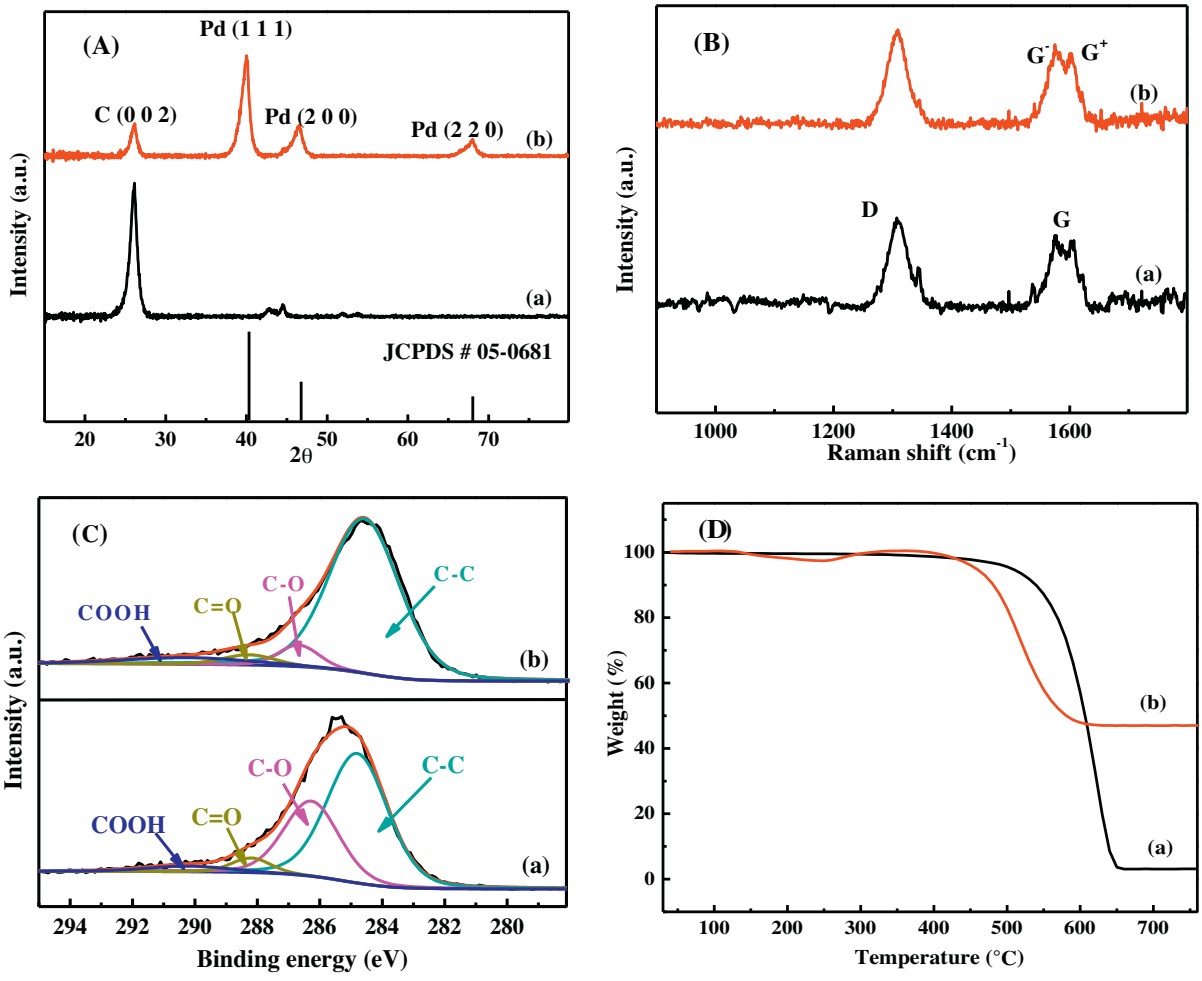

Fig. 1. (A) XRD pattern with standard card of Pd, (B) Raman spectra, (C) XPS curve fittings of the C1s and (D) TGA curves of (a) pure MWNTs and (b) Pd/MWNTs.

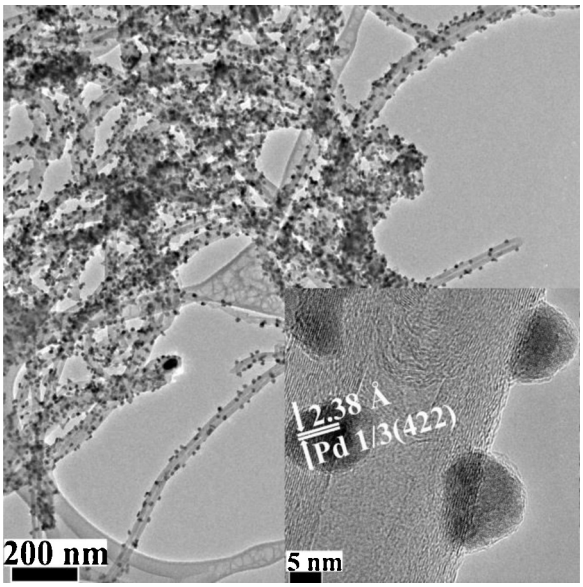

Fig. 2. TEM image of the synthesized Pd/MWNTs nanocatalysts, inset is the HRTEM image with clear lattice space.

3.2. TEM characterizations

The microstructure of the synthesized Pd/MWNTs is characterized by TEM (Fig. 2) and inset HRTEM image with clear lattice spacing. The Pd NPs are observed to be evenly distributed on the tube wall surface without obvious agglomeration due to the dispersion and anchoring role of functionalized carboxylic groups [42]. The microstructure of Pd NPs is further illustrated in the HRTEM image, the Pd NPs are uniformly distributed and anchored on the tube wall surface with an average size of 10 nm. The crystal structure is a key parameter that affects the catalytic activity of Pd toward FAOR. It is demonstrated by Nagahiro Hoshi et al. [47] that the catalytic activities of Pd with different crystal structures follow the order of Pd(1 1 0) < Pd(1 1 1) < Pd (1 0 0). In the synthesized Pd/MWNTs, a lattice space of 0.238 nm, characteristic of Pd(1 1 1) in the form of thin film and platelet due to 1/3(422) reflections, is observed from the HRTEM image [48]. Therefore, it can be inferred that the Pd in Pd/MWNTs is mostly (1 1 1) oriented.

3.3. Electrocatalytic evaluations

3.3.1. Electroactivity toward FAOR

Pd as a hydrogen storage material is well known to absorb massive quantities of hydrogen [49]. Fig. 3(a) shows the voltammetric behavior of the Pd/MWNTs electrode in 0.5 M H_2SO_4 at a scan rate of 50 mV s^{-1} with potential ranging from −0.4 to 1.0 V. The CV curve exhibits a single broad anodic peak (peak I) around −0.1 V due to the oxidation of both absorbed and adsorbed hydrogen on the Pd/MWNTs electrode. The cathodic peak (peak II) at −0.25 V during the reverse scan is assigned to reductive absorption and adsorption of hydrogen [50]. During the high potential range, Pd is oxidized to Pd(II) oxide and exhibits a broad peak around 0.8 V (peak III), the corresponding cathodic peak (peak IV) centering at 0.5 V is explained by the reduction of PdO. The electrochemically active surface area (*ECSA*) related with the active sites of catalyst and the conductive pathways available to transfer electrons from and to the catalyst surface is calculated to be 74.8 m^2 $g_{Pd}{}^{-1}$ from integrating peak IV using Eq. (1).

$$ECSA = Q/SL \quad (1)$$

where "*Q*" is the charge associated with PdO stripping, "*S*" is the proportionality coefficient as 405 μC cm^{-2}, which is used to relate charges with area under an assumption that a monolayer of PdO covers on the surface, '*L*' is the Pd loading in 'g'.

CV towards FAOR is conducted on the same Pd/MWNTs electrode in 0.5 M H_2SO_4 containing 0.2 M HCOOH ranging from −0.4 to 1.0 V, Fig. 3(b). The pair of hydrogen oxidation and reduction (centered at −0.1 and −0.25 V) is still observed when the potential ranges from −0.4 to 0 V, indicating that the corresponding hydrogen reactions are not fully depressed by the oxidation of HCOOH molecules. A further potential increase from 0 V leads to an obvious increase of current density, indicating the onset oxidation of HCOOH molecule. However, the increasingly produced CO_{ads} poisoning species are absorbed on the Pd surface and largely block the further oxidation of fresh HCOOH molecules causing a decline of the current density [51]. In addition, the oxidation of Pd to PdO during the high potential range also largely limits the electrocatalytic activity of Pd. The main oxidation peak observed at 0.23 V is assigned to the oxidation of fresh HCOOH and the minor hump at about 0.5 V indicates the oxidation of Pd [52,53]. The peak current density (j_p) of the Pd/MWNTs electrode is 0.65 A/mg $_{Pd}$ after the normalization to Pd mass. In addition, the CV curves with current density normalized to catalysts area are also provided in Fig. 3(c&d) to comprehensively evaluate the catalysts performance. During the negative scan, the sharp peak around 0.45 V is assigned to the oxidation of fresh HCOOH on the reduced clean Pd surface. This CV pattern is observed to be consistent with the typical CV of Pd (1 1 1) [47], also confirming the lattice space analysis in TEM.

3.4. Poisoning of Pd/MWNTs for FAOR

In order to further understand the poisoning mechanism of FAOR on the Pd-based catalysts, CV with different potential scan ranges on the Pd/MWNTs electrode are conducted in 0.5 M H_2SO_4 solution containing 0.2 M HCOOH at a scan rate of 50 mV s^{-1}. Fig. 4(A) shows the CV curves scanned from increased lowest potentials as (a) −0.4, (b) −0.1, (c) 0 and (d) 0.1 V to constant highest potential as 1.0 V. j_p as an important index to evaluate the activity of FAOR is observed to decrease first from 0.86 to 0.59 A/mg $_{Pd}$ when increasing the lowest potential from −0.4 to −0.1 V. However, further increasing the lowest potential to 0 and 0.1 V lead to an unchanged j_p value as 0.71 A/mg $_{Pd}$. The adsorbed hydrogen is well acknowledged to be essential for the commence of FA oxidation because it can facilitate the conversion of HCOOH molecules to a series of intermediates species such as $(COH)_{ads}$ and $[CH(OH)_2]_{ads}$ [40]. Since the hydrogen adsorption mainly proceeds before −0.1 V as confirmed from Fig. 3(a), it is deduced that the decreased j_p value is probably arising from the absence of the hydrogen adsorption in the low potential range, confirming the importance of adsorbed hydrogen in facilitating the FA oxidation. In order to investigate the role of high potential scan ranges during the FAOR, CV conducted with constant lowest potential as −0.4 V and increased the highest potential as (a) 0.3, (b) 0.4, (c) 0.6 and (d) 1.0 V are performed in Fig. 4(B). The j_p value is observed to decrease monotonously from 0.66 to 0.62 A/mg $_{Pd}$ when increasing the highest potential from 0.3 to 0.6 V. This can be explained from the aspect of CO_{ads} poisoning species. Since the adsorbed poisoning species are the main reason causing the decrease of current density and can only be oxidized during the high potential range, the CO_{ads} poisoning species will keep accumulating on the Pd surface and the increasingly serious poisoning phenomenon can't be alleviated due to the omission of high potential oxidation process. In contrast, a further increase of the potential to 1.0 V contributes to an obvious increase of j_p value from 0.59 to 0.68 A/mg $_{Pd}$, since the poisoning species have been totally oxidized in the high potential range, the produced clean Pd surfaces are responsible for this increased j_p

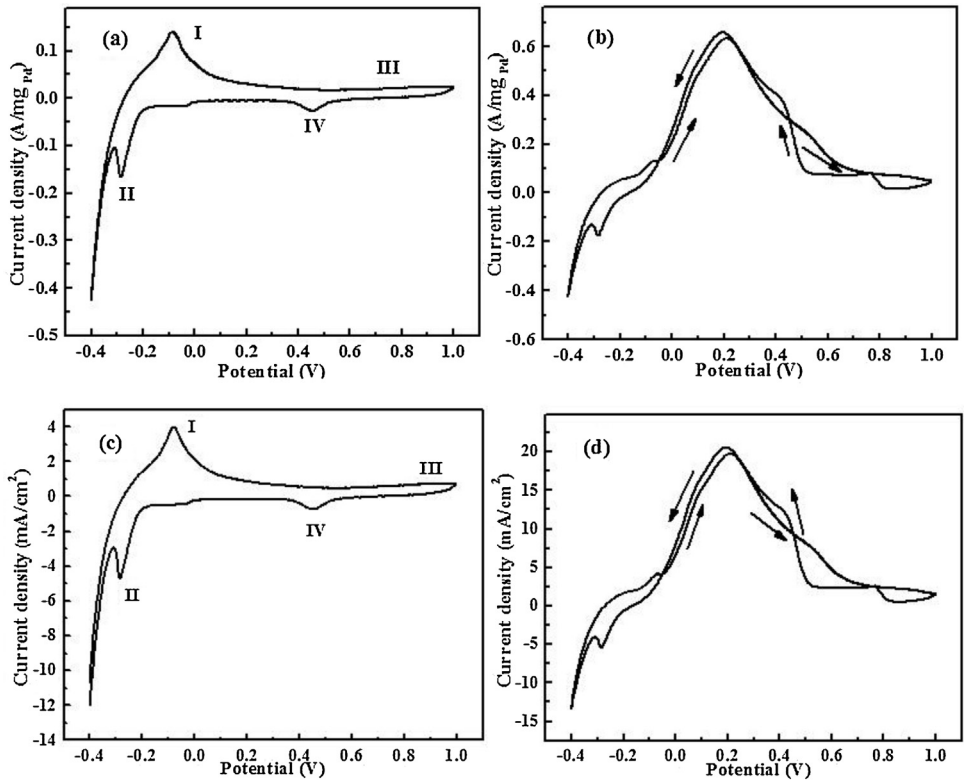

Fig. 3. CV of Pd/MWNTs in (a&c) 0.5 M H_2SO_4 solution, and (b&d) 0.5 M H_2SO_4 solution containing 0.2 M HCOOH. The scan rate is 50 mV/s, the current density is normalized to (a&b) Pd mass and (c&d) catalysts geometric surface area, respectively.

value. The positive roles of hydrogen adsorption at lower potentials and oxidation of CO_{ads} poisoning species at higher potentials are both confirmed again by a continuous 40 CV curves with different sweeping potential ranges as ten cycles each from 0.1 to 1.0 V, from −0.4 to 1.0 V, from −0.4 to 0.4 V and from −0.4 to 1.0 V. During these 40 CV cycles, overlapped curves are obtained during each 10 cycles within specific potential range, every tenth cycle of the corresponding potential range is recorded and shown in Fig. 4(C). The j_p value first increases from 0.47 to 0.53 A/mg $_{Pd}$ when expanding the potential range from 0.1 - 1.0 to −0.4 - 1.0 V, while a following decreased j_p value as 0.42 A/mg $_{Pd}$ is observed as the potential range is narrowed to −0.4 - 0.4 V. Finally, an increased j_p value as 0.46 A/mg Pd appears when the potential range is back to −0.4 - 1.0 V. However, it is clearly seen that the 40th j_p value (0.46 A/mg $_{Pd}$) is much lower than that of the 20th cycle (0.53 A/mg $_{Pd}$) with the same sweeping potential range (−0.4 to 1.0 V). In order to obtain detailed information about the decreased j_p value, CV was re-conducted in 0.5 M H_2SO_4 after performing all the above CV tests and compared with that in Fig. 3(a). The CV comparison is provided in Fig. 4(D), a largely decreased area of peak I is clearly seen after performing all the CVs due to the serious poisoning effect on the nanocatalysts. However, the unchanged peak IV implies a negligible effect of the detachment of Pd during the FAOR.

3.5. HCOOH concentration effect on FAOR

Fig. 5(A) displays the CV curves conducted in 0.5 M H_2SO_4 solution containing different HCOOH concentrations ranging from 0.2 to 12.0 M at a scan rate of 50 mV s^{-1}. The forward j_p value is observed to first increase from 0.65 to 1.38 A/mg $_{Pd}$ with increasing the HOOCH concentration from 0.2 to 4.0 M. However, further increasing HCOOH concentration to 12.0 M leads to an obviously decreased j_p value as 0.77 A/mg $_{Pd}$. Since HCOOH is the main electron donator during the oxidation process, it is reasonable that the j_p value will first increase with increasing the HCOOH concentration, however, as more and more poisoning species are produced and accumulated on the Pd surface when further increasing the HCOOH concentration, the continuous oxidation of HCOOH molecules will be largely blocked thus causing a decreased j_p value as indicated by the 12.0 M HCOOH. In addition, another important effect of increasing HCOOH concentration is on the difference between j_p values obtained from the forward and reverse scans. For 0.2 M HCOOH, Fig. 5A(a), the forward j_p value is almost the same as the reverse j_p value (0.65 A/mg $_{Pd}$), indicating an equivalent oxidation activity during the forward and backward sweeping. The reverse j_p is mainly related to the oxidation of fresh HCOOH molecules after the reduction of PdO to Pd, this reverse j_p value largely excludes the effect of CO_{ads} species in a very short period of time since CO_{ads} species have been totally oxidized during the high potential ranges. Therefore, it is deduced from the almost same forward and reverse j_p values that the CO_{ads} poisoning species are not playing a major role in decreasing the current density during the forward scan with low HCOOH concentrations. The less produced CO_{ads} poisoning species during forward scan are also consistent with the previous reports that FAOR is mainly proceeded through dehydrogenation pathway on Pd-based catalysts [54,55]. However, for 4.0 and 12.0 M HCOOH, Fig. 5A(b&c), the observed reverse j_p values (1.95 & 1.47 A/mg $_{Pd}$) greatly exceed the forward j_p values (1.38 & 0.779 A/mg $_{Pd}$) and the difference between them increases with increasing the HCOOH concentration. As the HCOOH molecules increase to a certain extent, the accumulated CO_{ads} poisoning species will influence the forward j_p significantly rather than the reverse j_p due to the full oxidization of poisoning species after sweeping through the high potential range. Therefore, the larger reverse j_p value can be probably attributed to the oxidation of fresh HCOOH molecules without the CO_{ads} poisoning effect in a short time. In summary, the enlarged j_p difference clearly indicates a worse poisoning phenomena and the

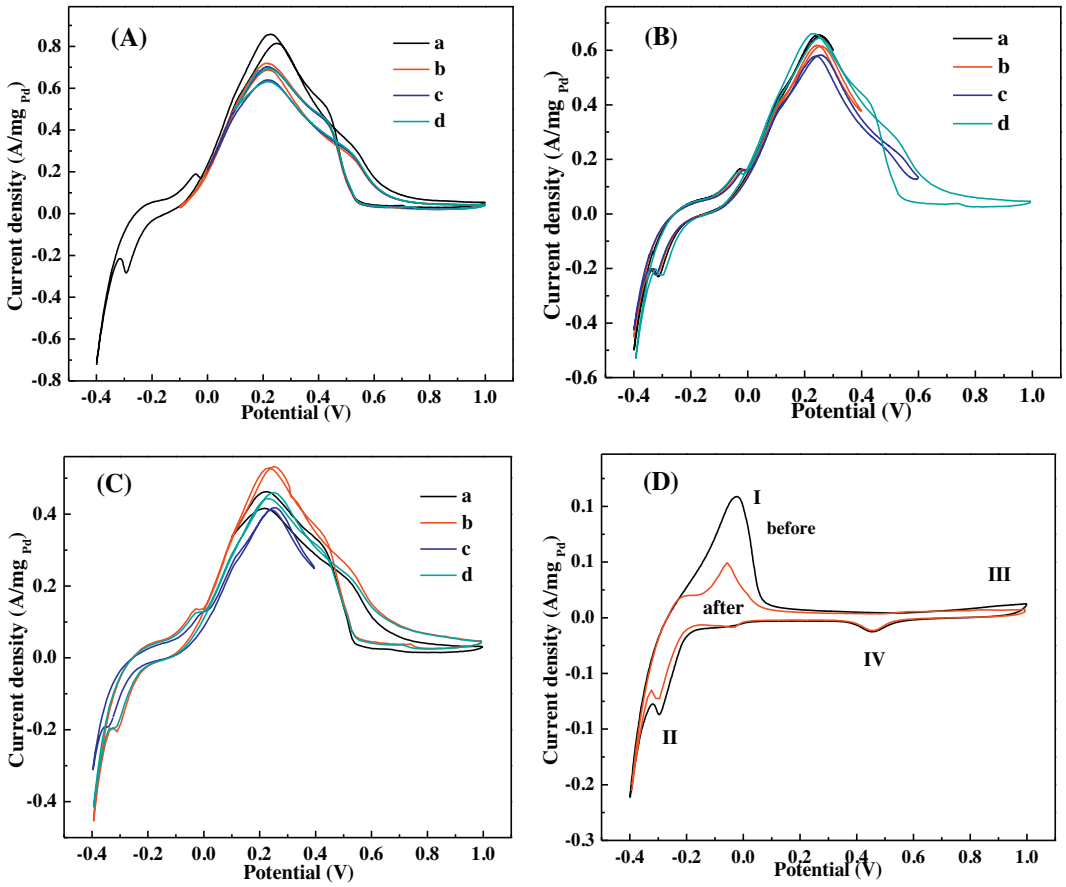

Fig. 4. CV of the Pd/MWNTs electrode in 0.5 M H_2SO_4 solution containing 0.2 M HCOOH at 50 mV s^{-1} with different sweeping potential ranges as (A) different lowest potential (a) −0.4, (b) −0.1, (c) 0 and (d) 0.1 V with constant highest potential 1.0 V, (B) different highest potential (a) 0.3, (b) 0.4, (c) 0.6 and (d) 1.0 V with constant lowest potential as −0.4 V and (C) four selected CV curves from 40 continuous CV curves with different potential ranges (10 cycles for each) as (a) 10th cycle with potential sweeping from 0.1 to 1.0 V, (b) 20th cycle with potential sweeping from −0.4 to 1.0 V, (c) 30th cycle with potential sweeping from −0.4 to 0.4 V and (d) 40th cycle with potential sweeping from −0.4 to 1.0 V, (D) Comparison of CV curves in 0.5 M H_2SO_4 solution before and after all the above CV tests with current density normalized to Pd mass at 50 mV s^{-1}.

dehydration pathway plays an increasing role during FAOR when increasing the HCOOH concentration.

Slow linear sweep voltammetry (SLV) as a useful tool to investigate the inner oxidation mechanism of FAOR was also conducted from −0.2 to 0.8 V at a scan rate of 1.0 mV s^{-1} in the corresponding electrolytes, Fig. 5(B). For 0.2 M HCOOH, only one dominant peak is clearly seen around 0.1 V, suggesting that the HCOOH molecules are mainly oxidized through the dehydrogenation pathway in low HCOOH concentration electrolytes, which is also consistent with the CV results. However, two peaks observed around 0.1 and 0.7 V representing dehydrogenation and dehydration pathways are clearly seen with 4.0 M HCOOH, indicating a clear variation of the oxidation mechanism. i.e., from main dehydrogenation pathway for low HCOOH concentration to combined dehydrogenation with dehydration pathways for high HCOOH concentration. Furthermore, the second peak is observed to become relatively dominant with increasing the HCOOH concentration from 4.0 to 12.0 M. The increased peak II/I ratio demonstrates that increasing the HCOOH concentration can direct increase the proportion of dehydration pathway to dehydrogenation pathway. In addition, it's clearly seen from Fig. 5(B) that the peak current potential (E_p) of peak I negatively shift with increasing the HCOOH concentration, indicating an easier dehydrogenation process due to the increased availability of fresh HCOOH molecules, however, the positive shifted onset potential of peak II of 12.0 M HCOOH is probably due to the relatively decreased H^+. Finally, an obvious intensity decrease of peak I is clearly observed for 12.0 M HCOOH, suggesting an largely decreased dehydrogenation process by the increased CO_{ads} poisoning species and a shift from dehydrogenation process to dehydration process with increasing the HCOOH concentration. The kinetics of FAOR at different HCOOH concentrations were also studied via Tafel analysis, Fig. 5(C). All of the curves were fitted and divided into two parts representing dehydrogenation and dehydration processes. It is clearly seen that at the lowest concentration of HCOOH, 0.2 M, the Tafel plot exhibits the lowest slope (102.6 mV/dec) for dehydrogenation process and a negative slope for dehydration process, implying a dominated dehydrogenation pathway and a negligible dehydration pathway at low HCOOH concentrations. The slope of dehydrogenation increases to 134 and 184.5 mV/dec with increasing the HCOOH concentration to 4.0 and 12.0 M, respectively, suggesting a deteriorated dehydrogenation pathways due to the increased poisoning species. In addition, enhanced dehydration pathway with increasing the HCOOH concentration from 4.0 to 12.0 M is also obtained from the decreased slope, confirming again that increasing the HCOOH concentration can directly increase the dehydration proportion.

In order to further probe the tolerance stability and the inherent kinetics variation with different HCOOH concentrations, CA and EIS characterizations of the Pd/MWNTs electrode were conducted in 0.5 M H_2SO_4 solution containing a HCOOH concentration of (A&D) 0.2, (B&E) 6.0 and (C&F) 12.0 M, Fig. 6. CA was carried out at a potential of (a) 0, (b) 0.2, (c) 0.4 and 0.6 V each for a duration of 300 s. The selected potentials represent four regions, i.e., the onset

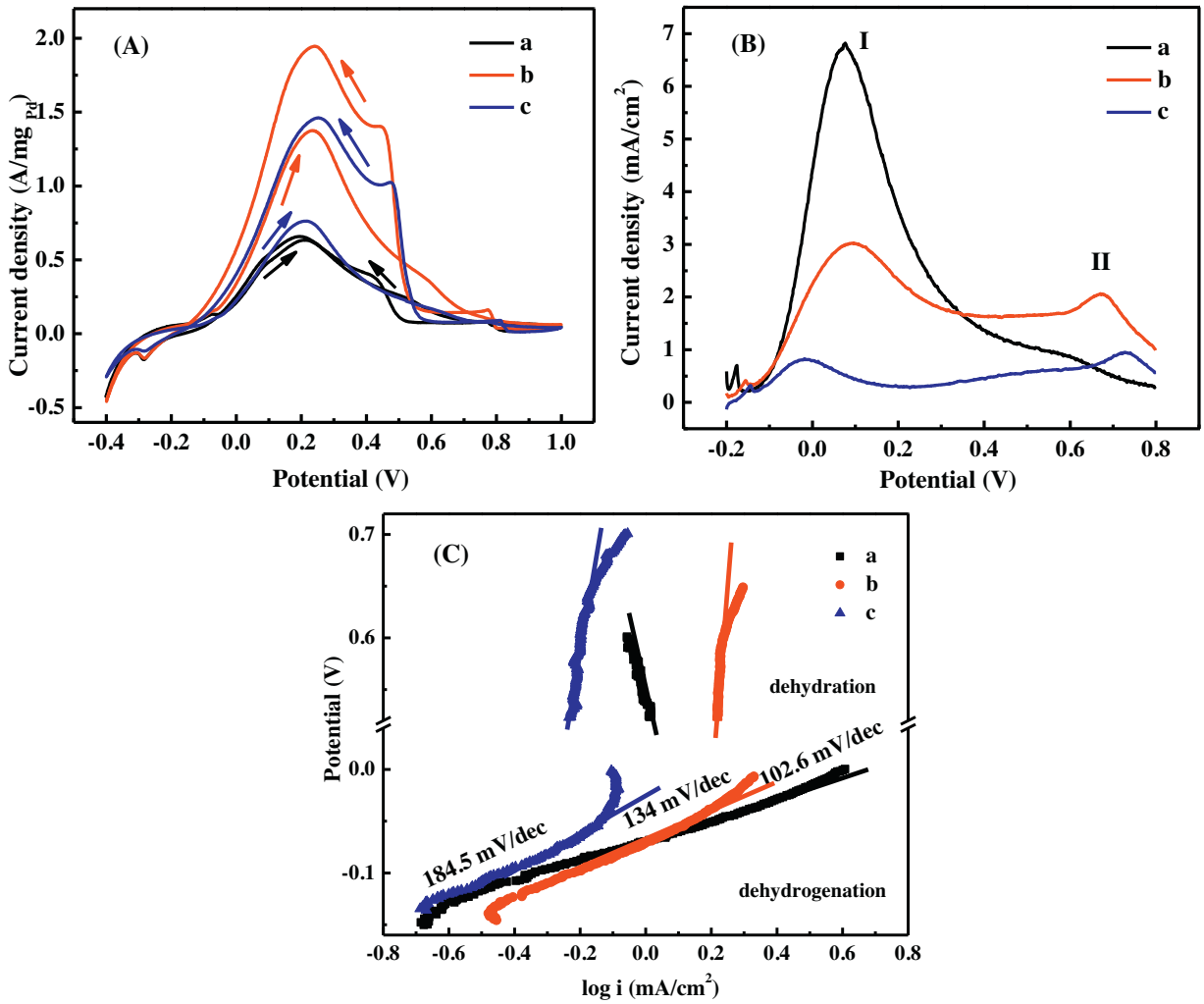

Fig. 5. (A) CV at 50 mV s^{-1}, (B) LSV at 1.0 mV s^{-1} and (C) Tafel of the Pd/MWNTs electrode in 0.5 M H_2SO_4 solution containing HCOOH concentration as (a): 0.2, (b): 4.0 and (c):12.0 M.

oxidation of HCOOH through dehydrogenation pathway, the peak of HCOOH dehydrogenation pathway, the onset oxidation of HCOOH through dehydrogenation pathway and the peak of HCOOH dehydration pathway. For 0.2 M HCOOH, Fig. 6(A), the CA at 0.2 V maintains the lowest decay rate and the highest extreme current density, suggesting a dominant dehydrogenation pathway. However, for CA curves of 4.0 and 12.0 M HCOOH, Fig. 6(B&C), fast decays are both observed at 0.2 V, implying serious CO_{ads} poisoning effects during the dehydrogenation process. In contrast, the extreme currents at 0.4 and 0.6 V are observed to maintain relatively higher values and lower decay rates, suggesting the shift of reaction pathway from dehydrogenation to dehydration pathway with increasing the HCOOH concentration.

EIS as a useful technique providing valuable information about the inherent kinetics of electro-transfer process was carried out in the frequency range from 100 000 to 0.01 Hz with a 5 mV amplitude for different HCOOH concentrations. Nyquist impedance plots of different HCOOH concentrations with potential varying from −0.2 to 0.9 V (shown as Figure legends) are provided in Fig. 6(D–F). For 0.2 M HCOOH, Fig. 6(D), the impedance arcs from −0.2 to 0.1 V (all located in the first quadrant) decrease monotonously with increasing the potential. The observed monotonously decreased impedance arcs from −0.2 to 0.1 V is an indicator of onset oxidation of HCOOH [56]. A rapid slope increase of the liner portion part is observed as the potential is increased to 0.2 V, indicating the appearance of an increasingly dominant diffusion-controlled component due to the potential-enhanced electron-transfer kinetics [57]. The arcs begin to bend to the second quadrant and increase monotonously with the potential sweeping from 0.3 to 0.6 V. The negative faradaic impedance suggests the presence of an inductive component as a consequence of the oxidative removal of the adsorbed CO_{ads} species on the Pd surface by the chemisorbed $OH_{ads,}$ which is regarded as the rate-determining step during this potential range [57]. The arcs begin to return to the first quadrant when the potential is higher than 0.5 V, suggesting a variation of the rate-determining step, since the electro-oxidation of surface adsorbed CO_{ads} will be drastically accelerated during this potential region, the formation of CO_{ads} through dehydration pathway appears to become the rate-determining step [57]. This interesting impedance pattern variation has also been reported by numerous works [58–60]. For HCOOH oxidation with higher HCOOH concentrations, i.e., 6.0 and 12.0 M, similar patterns to that of 0.2 M HCOOH are observed, Fig. 6(E&F), the arc diameters decrease first when the potential increases within the range from −0.2 to 0.1 V, the arcs then bend to the second quadrant and finally back to the first quadrant. However, the arcs are observed to reach the forth quadrant within the potential range at 0.2 V for 6.0 M HCOOH and

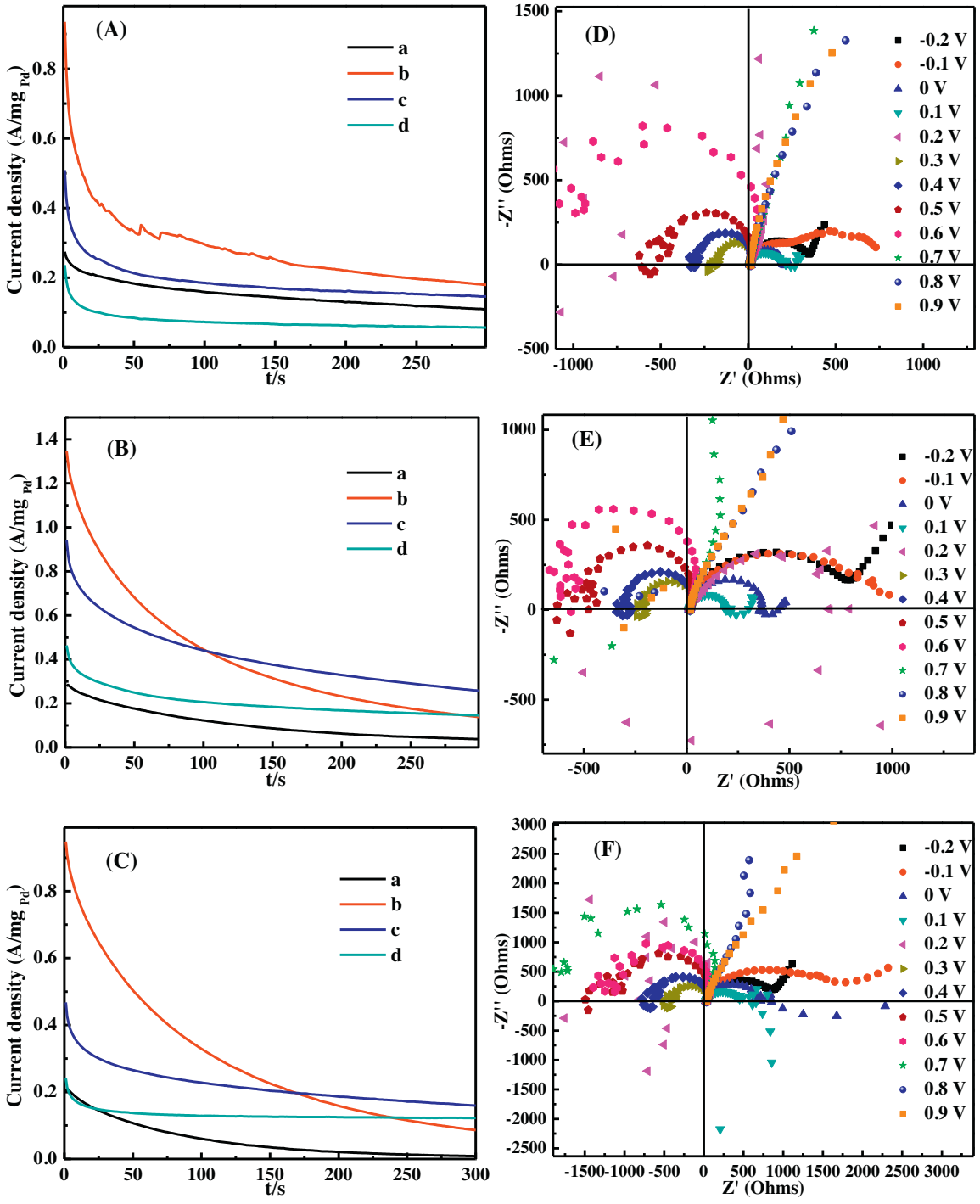

Fig. 6. CA and EIS of the Pd/MWNTs electrode in 0.5 M H_2SO_4 solution containing HCOOH concentration as (A&D) 0.2, (B&E) 4.0 and (C&F) 12.0 M. CA (A–C) was conducted at a potential of (a) 0, (b) 0.2, (c) 0.4 and (d) 0.6 V, EIS (D–F) was conducted at various electrode potentials (−0.2 - 0.9 V) as shown in the Figure legends.

0.1 V for 12.0 M HCOOH, respectively, indicating the presence of a small pseudoinductive component due to the oxidative removal of adsorbed CO_{ads} species [57]. The early appearance of this pseudoinductive component demonstrates the easier oxidation of the produced CO_{ads} species with increasing HCOOH concentration. Based on the impedance results and above analysis, two equivalent circuits, Fig. S1, are used to fit the EIS positive and negative impedances, respectively. The fitting circuit of positive impedance part is provided in Fig. S1(A), normal components as R_s represents the solution resistance, *CPE* for constant-phase element and R_{ct} for the charge-transfer resistance evaluating how fast the charge transfer during the oxidation process. However, a more complex model, Fig. S1(B), is employed for the fitting of negative impedance part, where newly employed C_0 and R_0 represent the capacitance and resistance of the electrooxidation of adsorbed CO_{ads} intermediates [59]. The R_{ct} fitting results are provided in Fig. S2. Both rough increase trends of R_{ct} value are clearly observed in negative and positive ranges with increasing the HCOOH concentration. The observed harder oxidation process is caused by the increased poisoning effect, indicating an increased proportion of dehydration pathway to dehydrogenation pathway with increasing the HCOOH concentration.

3.6. H_2SO_4 concentration effect on FAOR

Similar to the HCOOH concentration effect on FAOR, H_2SO_4 concentration effect on FAOR was also studied in order to provide a favorable environment for FAOR. Fig. 7 illustrates the CV and LSV curves of the Pd/MWNTs electrode in 4.0 M HCOOH aqueous solution with varying H_2SO_4 concentration from 0 to 4.0 M. The observed forward j_p value in Fig. 7(A) first increases from 0.92 to 1.38 A/mg $_{Pd}$ with increasing the H_2SO_4 concentration from 0 to 0.5 M and a great decreased j_p value (0.37 A/mg $_{Pd}$) is observed when further increasing the H_2SO_4 concentration to 4.0 M. The first increased j_p value confirms the positive role of H^+ in facilitating the FAOR in low H_2SO_4 concentration solution, which is probably due to the reactant role of H^+ during FAOR [61]. However, the declined j_p value in the electrolyte with 4.0 M H_2SO_4 demonstrates that an excessive amount of H_2SO_4 can reversely depress the HCOOH oxidation. Since H^+ has to be extracted from HCOOH molecules during the FAOR in spite of dehydrogenation or dehydration pathway, it is reasonable the excess H^+ will make the oxidation process hard to proceed due to the extremely unbalanced equilibrium of H^+. In addition, the increased adsorption of bisulfate anions can also inhibit the reaction [62,63]. An obvious negative shift of E_p with increasing H_2SO_4 concentration is also clearly seen in Fig. 7(A), indicating an easier onset oxidation of HCOOH molecules with increased H^+. For FAOR in 4.0 M HCOOH solution without H_2SO_4, Fig. 7A(a), a slow current increase trend is clearly seen when increasing the potential from −0.2 to 0.6 V, a sharp current decrease is following observed starting around 0.6 V due to the Pd oxidation which results a much higher E_p value compared with the electrolytes containing H_2SO_4. The extremely positive shifted E_p value indicates a sluggish kinetics and the decrease of current density is mainly attributed to the oxidation of Pd. In addition, a sharp increase of current density is also observed at 0.55 V during the negative scan, different from the electrolytes with H_2SO_4. The sharp increase is explained by the preliminary oxidation of fresh HCOOH molecules on the total re-cleaned Pd surface without further oxidation in the absence of H^+ [41]. The potential where the sharp increase occurs is also consistent with the Pd reduction potential during the negative scan. In contrast, for electrolyte with H_2SO_4, gradual increases of current density during the reverse scan are observed due to the further oxidation of the produced intermediates on the re-cleaned Pd sites in the presence of abundant H^+.

In order to gain an insight into the inherent mechanism variation, LSV of the Pd/MWNTs electrode were also performed in 0, 0.5 and 4.0 M H_2SO_4 solution containing 4.0 M HCOOH ranging from −0.8 to 0.2 V at a scan rate of 1 mV s^{-1} as shown in Fig. 7(B). Similar peaks as I and II are assigned to the dehydrogenation and dehydration pathways, indicating the existence of dual pathways regardless of the variation of H_2SO_4 concentration. For electrolyte without H_2SO_4, Fig. 7B(a), peak II is comparable with that of peak I, suggesting that the dehydration pathway plays a comparable role to the dehydrogenation pathway during the FAOR. However, for electrolyte with 0.5 M H_2SO_4, Fig. 7B(b), the ratio of peak II/I is largely decreased, implying that the main pathway is shift to dehydrogenation when increasing H^+. However, both peaks are largely depressed when the H_2SO_4 concentration increased to 4.0 M due to the excess H^+ and largely adsorbed bisulfate anions, which is also consistent with the CV results. The Tafel curves were also provided in Fig. 7(C) to study the kinetics at different H_2SO_4

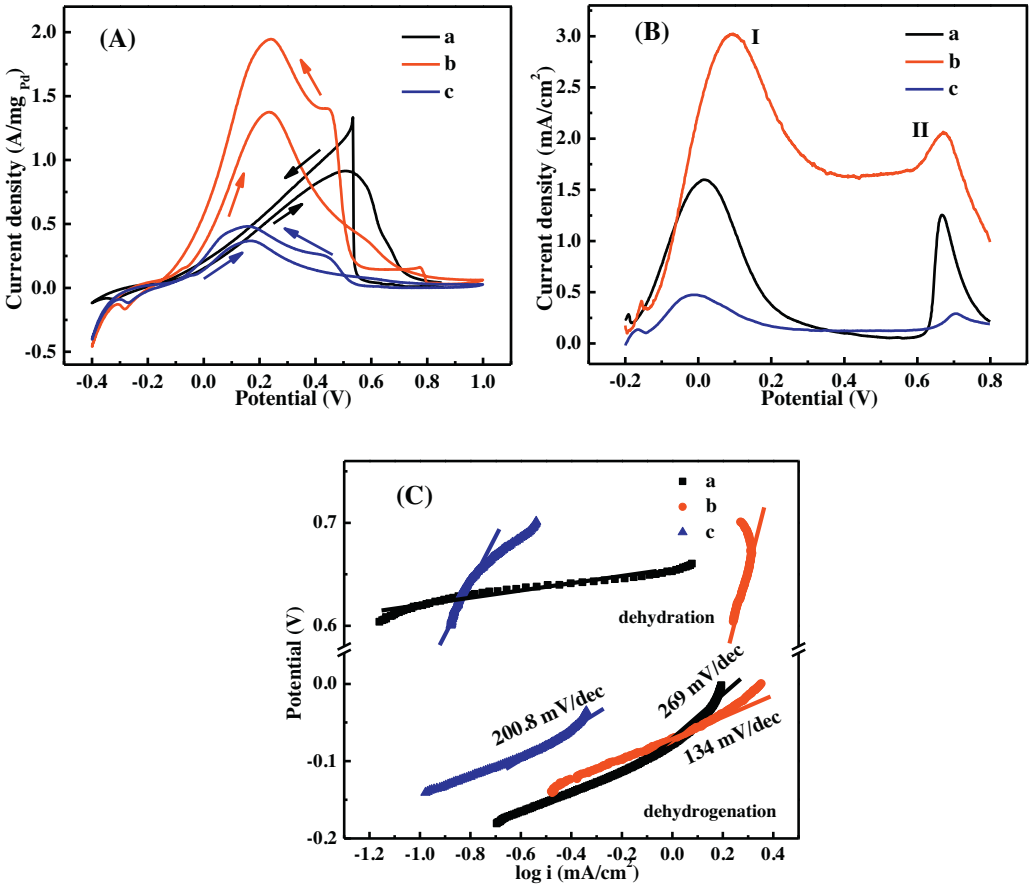

Fig. 7. (A) CV at 50 mV s^{-1}, (B) LSV at 1.0 mV s^{-1} and (C) Tafel of the Pd/MWNTs electrode in solutions containing 4.0 M HCOOH with H_2SO_4 concentration as (a) 0, (b) 0.5 and (c) 4.0 M.

concentrations. It is clearly seen that at 0 M, the Tafel curve exhibits the highest slope for dehydrogenation process and the lowest slope for dehydration pathways, indicating a suppressed dehydrogenation pathway and an enhanced dehydration pathway without H_2SO_4. When increase the H_2SO_4 concentration to 0.5 M, the slope for dehydrogenation process is decreased to 134 mV/dec, suggesting a positive role of H^+ in promoting dehydrogenation pathway at low H_2SO_4 concentrations. Interestingly, the slope is increased to 200.8 mV/dec when further increasing the concentration of H_2SO_4 to 4.0 M, implying a negative effect of high H_2SO_4 concentrations, which agrees well with the CV and LSV measurements. Finally, the slope of the dehydration process is observed to decrease when continue increasing the H_2SO_4 concentration from 0.5 to 4.0 M, implying a facilitating role of H^+ in oxidizing poisoning species.

Similar to the characterization of HCOOH concentration effect, CA and EIS techniques were also employed to investigate the variations of tolerance stability and inherent reaction kinetics with varying H_2SO_4 concentration. Fig. 8(A–C) displays the CA conducted at a potential of (a) 0, (b) 0.2, (c) 0.4 and (d) 0.6 V for a duration of 300 s in (A) 0, (B) 0.5 and (C) 4.0 M H_2SO_4 solution containing 4.0 M HCOOH. For the CA without H_2SO_4, Fig. 8(A), the current density at 0.2 and 0.4 V exhibit relatively quick decays compared with that of 0.5 and 4 M H_2SO_4, indicating a bad tolerance stability and a largely depressed dehydrogenation pathway. However, the CA curve at 0.4 V exhibits a relatively low decaying rate and maintains the highest extreme current density after introducing 0.5 M H_2SO_4, Fig. 8(B), the observed increasingly dominant dehydrogenation pathway confirms the

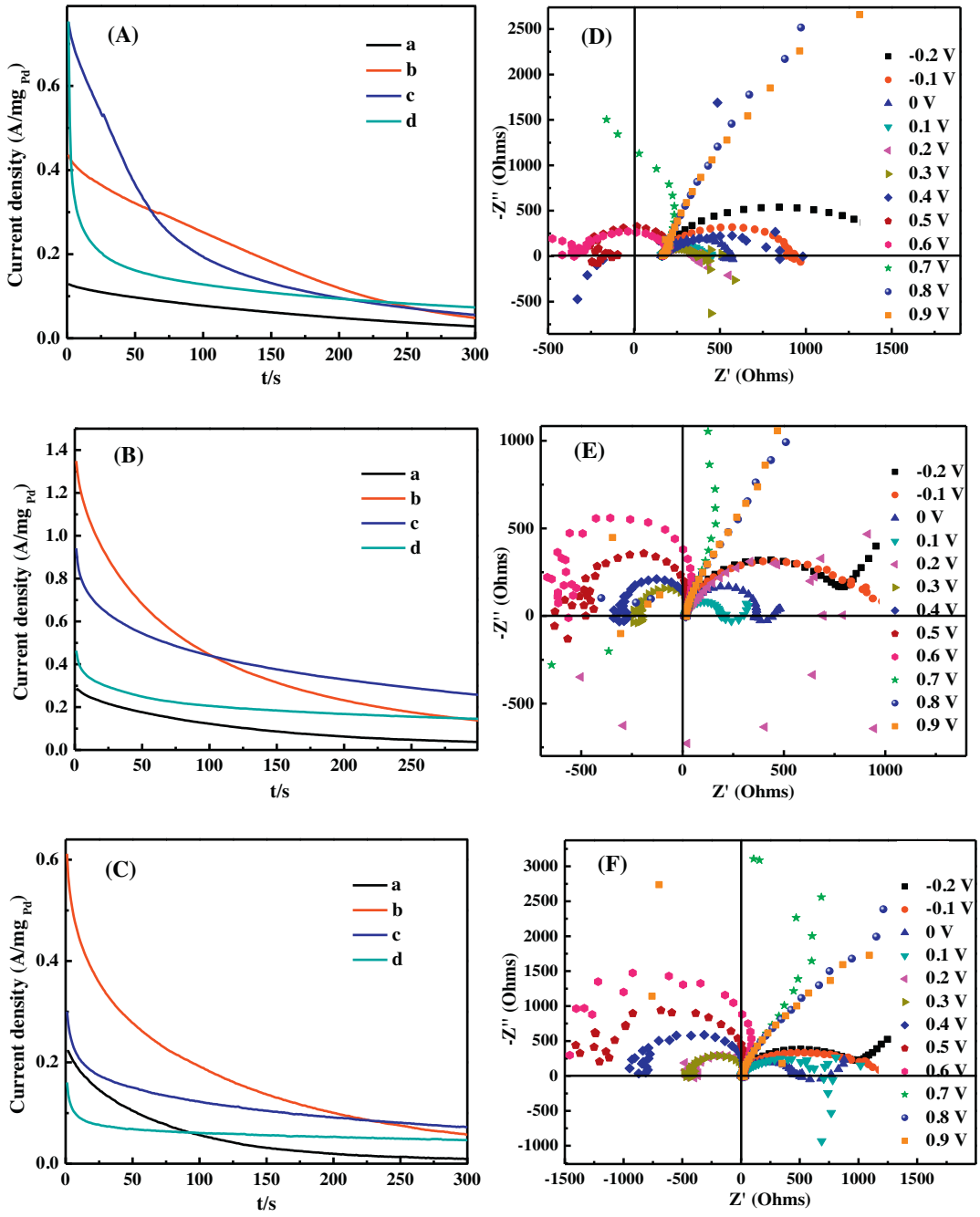

Fig. 8. CA (A–C) at a potential of (a) 0, (b) 0.2, (c) 0.4 and (d) 0.6 V as well as EIS (D–F) at various electrode potentials ranging from −0.2 to 0.9 V conducted on the Pd/MWNTs electrode in different electrolytes containing 4.0 M HCOOH with H_2SO_4 concentration as (A&D) 0, (B&E) 0.5 and (C&F) 4.0 M.

facilitating role of increasing H^+ to dehydrogenation pathway. Finally, it is observed from Fig. 8(C) that all the current densities for 4.0 M H_2SO_4 is much lower than that of 0.5 M H_2SO_4, indicating a low tolerance stability in the solutions at high H_2SO_4 concentrations.

The EIS curves conducted at various potentials ranging from −0.2 to 0.9 V in 0, 0.5 and 4.0 M H_2SO_4 solutions containing 4.0 M HCOOH are provided in Fig. 8(D–F). For the EIS curve without H_2SO_4, Fig. 8(D), the potential range from −0.2 to 0.2 V where the arc diameter decrease happens is observed to be much wider than that with H_2SO_4 in electrolyte (from −0.2 to 0.1 V for 0.5 M H_2SO_4 and from −0.2 to 0 V for 4.0 M H_2SO_4). The wider potential range where the onset oxidation of HCOOH happens indicates a sluggish kinetics caused by the absence of H_2SO_4 within the low potential ranges. Furthermore, the intercept of the EIS curve with x-axis represents the equivalent series resistance (*ESR*), which mainly arises from the electrolyte resistance since the catalyst effect is excluded [64]. It is clearly seen from Fig. 8(D–E) that the *ESR* value of 0 M H_2SO_4 (245 Ω) is much higher than that of 0.5 and 4.0 M H_2SO_4 (0 Ω), indicating a higher electrolyte resistance without H_2SO_4. For HCOOH oxidation in 0.5 and 4.0 M H_2SO_4, the minimum arcs are observed at 0.1 and 0 V, respectively, both lower than that without H_2SO_4 (0.2 V) and decrease with increasing H_2SO_4 concentration, demonstrating a facilitating role of increasing H^+ to the onset oxidation of HCOOH. In addition, the small pseudoinductive component representing the removal of CO_{ads} species which is determined from the extension of arc to the fourth quadrant appears more negative with increasing the H_2SO_4 concentration, i.e., 0.3 V for 0 M H_2SO_4, 0.2 V for 0.5 M H_2SO_4 and 0.1 V for 4.0 M H_2SO_4. The decreased potential indicates an earlier removal of CO_{ads} poisoning species with increasing the H_2SO_4 concentration, demonstrating a promotion effect of H^+ on the removal of CO_{ads} species and also consistent with Tafel results. The EIS curves are also curve fitted using the two equivalents presented in Fig. S1 and the obtained variation trends of R_{ct} with potential results are given in Fig. S3. Similar trends of R_{ct} v.s. potential with different H_2SO_4 concentrations are observed. However, a clear negative shift of the trend is clearly seen with increasing H_2SO_4 concentration, implying that the onset oxidation of HCOOH can be made easier when increasing H^+. In addition, the absolute R_{ct} values after 0.2 V increase largely with increasing the H_2SO_4 concentration, indicating a slow charge transfer reaction kinetics due to the excess H^+ and bisulfate anions and also consistent with the CV and LSV analysis.

3.7. Temperature effect on FAOR

Three temperatures of 2, 22, and 40 °C representing cold, normal and hot weather were selected to probe the temperature effect on the catalytic activity and inherent reaction kinetics of Pd/MWNTs for FAOR. Fig. 9 depicts the similar characterizations of the Pd/MWNTs electrode applied with different temperatures in 0.5 M H_2SO_4 solution containing 0.2 M HCOOH at scan rates of 50 and 1.0 mV s^{-1}, respectively. For the CV characterization, Fig. 9(A), the observed largely increased j_p value indicates the positive role of increasing the temperature in facilitating the oxidation of HCOOH. The j_p value is observed to increase almost seven times (from 0.19 to 1.24 A/mg $_{Pd}$) as the temperature increases from 2 to 40 °C. In addition, the onset potential of the HCOOH oxidation is also observed to negative shift with increasing the HCOOH

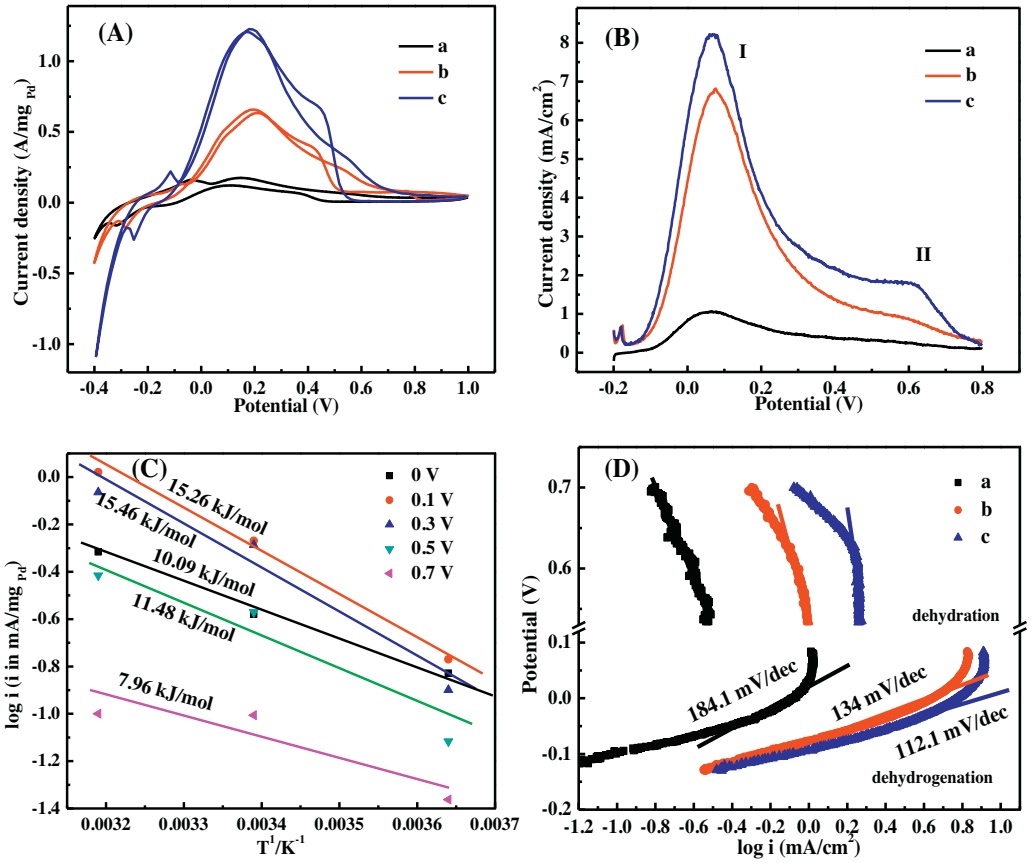

Fig. 9. (A) CV at 50 mV s^{-1}, (B) LSV at 1.0 mV s^{-1}, (C) Arrhenius plots of log i versus 1/T at different potentials and (D) Tafel of Pd/MWNTs electrode in 0.5 M H_2SO_4 solution containing 0.2 M HCOOH at (a) 2, (b) 22, and (c) 40 °C.

concentration, suggesting a much easier oxidation with increasing the temperature. Fig. 9(C) shows the relationship between log i and 1/T for FAOR at five selected potentials. The rough linear relationship suggests that the reaction mechanism at each potential does not change with varying temperature. The apparent activation energies, E_a, is also calculated and provided correspondingly at each potential in Fig. 9(C). The E_a at 0.1 and 0.3 V was calculated to be 15.26 and 15.46 kJ/mol, much higher than that of other potentials, indicating high sensitivity of dehydrogenation process to temperature. For the LSV characterization, Fig. 9(B), a similar current density increase is clearly seen, consistent with the CV results. For HCOOH oxidation at 2 and 22 °C, peak I is only observed, implying the dominant dehydrogenation pathway. However, peak II assigned to the dehydration pathway appears when the temperature is increased to 40 °C, indicating an increased role of dehydration pathway when increasing the temperature. Since the reaction kinetics of HCOOH oxidation can be greatly increased at high temperatures, the CO_{ads} species are more easily produced through dehydration pathway thus contributing to the appearance of peak II. The kinetics study of temperature effect toward FAOR was also performed through Tafel, Fig. 9(D). Pd/MWNTs exhibit the largest slope (181.4 mV/dec) for

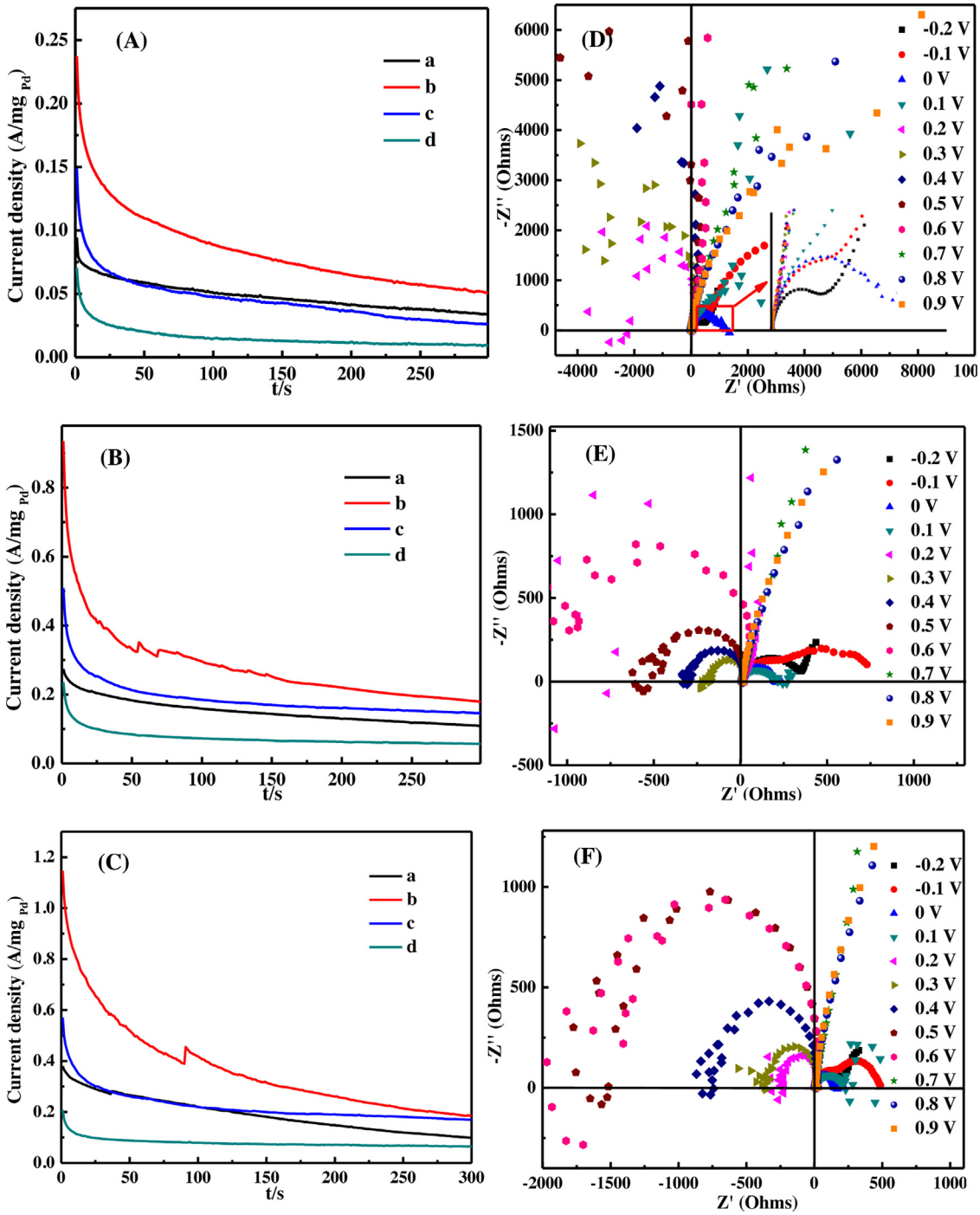

Fig. 10. CA (A–C) at a potential of (a) 0, (b) 0.2, (c) 0.4 and (d) 0.6 V as well as EIS (D–F) at various electrode potentials ranging from −0.2 to 0.9 V conducted on the Pd/MWNTs electrode in 0.5 M H_2SO_4 solution containing 0.2 M HCOOH at different temperatures as (A&D) 2, (B&E) 22 and (C&F) 40 °C.

dehydrogenation pathway at 0 °C, indicating a sluggish reaction kinetics. The slopes of the dehydrogenation pathway lower to 134 and 112.1 mV/dec with increasing the temperature to 22 and 40 °C, respectively, can be explained by the enhanced ion mobility. Besides, negative slopes of dehydration pathway are observed at all these three temperatures, nevertheless, the decreased slopes with increasing the temperature confirm an increased dehydration pathway.

Detailed study about the temperature effect on the tolerance stability and reaction kinetics were performed through CA and EIS characterizations similarly. Fig. 10 depicts the CA curves conducted at a potential of 0, 0.2 0.4 and 0.6 V and the EIS Nyquist plots performed at various potentials ranging from −0.2 to 0.9 V in 0.5 M H_2SO_4 solution containing 0.2 M HCOOH at (A&D) 2, (B&E) 22 and (C&F) 40 °C. For the CA characterization, Fig. 10(A–C), the general extreme current densities follow an order as $2 < 22 < 40$ °C, confirming the positive effect of increasing the temperature on tolerance stability. In addition, the increasingly dominant role of dehydration pathway at 40 °C is also demonstrated by the relatively faster and slower decay rates at 0.2 V and 0.4 V as well as the roughly equal extreme current densities for 0.2 and 0.4 V at 300 s. For EIS characterization, Fig. 10(D–F), the arc diameter decreases first with increasing the potential in the first quadrant, then the pseudoinductive component appears as further increasing the potential, the arc diameters increase with increasing the potential in the second quadrant and finally return to the first quadrant. However, for HCOOH oxidation at 2 °C, Fig. 10(D), a slight arc diameter increase representing CO species removal is first observed with increasing the potential from −0.2 to 0.1 V as illustrated by the enlarged part inset of Fig. 10(D) [57,59]. This newly appeared arc diameter increase phenomenon is different from the arc diameter decrease trends for 22 and 44 °C, indicating sluggish reaction kinetics of Pd/MWNTs at low temperatures. For HCOOH oxidation at 22 and 40 °C, Fig. 10(E&F), the minimum arcs during the diameter decrease trend are obtained at 0.1 and 0 V, however, no comparable value is found for 2 °C due to the disappearance of diameter decrease trend in the first quadrant, suggesting that the production and removal of CO_{ads} is more easily proceeded when increasing the temperature. Finally, the R_{ct} values obtained from the fitted EIS curves are also provided in Fig. S4, For FAOR at 2 °C, Fig. S4(a), the absolute R_{ct} values of 2 °C are much higher than that of 22 and 40 °C during the low potential range due to the sluggish reaction kinetics. Since the mobility of ions is greatly facilitated at higher temperatures, the reaction kinetics are greatly enhanced as confirmed by the decreased R_{ct} values for 22 and 40 °C in Fig. S4(b&c).

4. Conclusions

Pd/MWNTs nanocatalysts were employed as a representative Pd-based catalyst to investigate the FAOR mechanism and poisoning effect on the Pd/MWNTs electrode in H_2SO_4 solution. The hydrogen adsorption in low potential range and the oxidation of poisoning species during the high potential range both contribute to the enhanced electroactivity of Pd/MWNTs. The dual pathway mechanism is comprehensively studied by CA and EIS, indicating that the oxidation of HCOOH through dehydrogenation pathway only proceeded in conditions with relatively lower HCOOH and H_2SO_4 concentrations. Increasing HCOOH concentration can directly increase the dehydration process proportion and cause the increase of CO_{ads} species. H_2SO_4 as donor of H^+ can greatly facilitate the onset oxidation of HCOOH in the beginning process, but it will largely depress the HCOOH oxidation with excess amount of H^+. Finally, increasing temperature can boast the mobility of ions and thus enhance the reaction kinetics as well as cause the appearance of dehydration process.

Acknowledgements

The financial supports from University of Tennessee Knoxville are kindly acknowledged. Dr. Z. Wang acknowledges NIH under Grant 2G12MD007595–06 for support.

Appendix A. Supplementary data

Supplementary data associated with this article can be found, in the online version, at http://dx.doi.org/10.1016/j.electacta.2015.10.046.

References

[1] E. Antolini, E.R. Gonzalez, Alkaline direct alcohol fuel cells, J. Power Sources 195 (2010) 3431–3450.
[2] E.H. Yu, U. Krewer, K. Scott, Principles and Materials Aspects of Direct Alkaline Alcohol Fuel Cells, Energies 3 (2010) 1499–1528.
[3] Y. Zhu, S.Y. Ha, R.I. Masel, High power density direct formic acid fuel cells, J. Power Sources 130 (2004) 8–14.
[4] S. Wang, X. Wang, S.P. Jiang, Controllable self-assembly of Pd nanowire networks as highly active electrocatalysts for direct formic acid fuel cells, Nanotechnology 19 (2008) 455602.
[5] G. Hu, F. Nitze, H.R. Barzegar, T. Sharifi, A. Mikołajczuk, C.-W. Tai, et al., Palladium nanocrystals supported on helical carbon nanofibers for highly efficient electro-oxidation of formic acid, methanol and ethanol in alkaline electrolytes, J. Power Sources 209 (2012) 236–242.
[6] C. Venkateswara Rao, C.R. Cabrera, Y. Ishikawa, Graphene-Supported Pt–Au Alloy Nanoparticles: A Highly Efficient Anode for Direct Formic Acid Fuel Cells, J. Phys. Chem. C 115 (2011) 21963–21970.
[7] C. Rice, S. Ha, R.I. Masel, P. Waszczuk, A. Wieckowski, T. Barnard, Direct formic acid fuel cells, J. Power Sources 111 (2002) 83–89.
[8] M. Zhao, C. Rice, R.I. Masel, P. Waszczuk, A. Wieckowski, Kinetic Study of Electro-oxidation of Formic Acid on Spontaneously-Deposited Pt/Pd Nanoparticles, J. Electrochem. Soc. 151 (2004) A131–A136.
[9] C. Rice, Catalysts for direct formic acid fuel cells, J. Power Sources 115 (2003) 229–235.
[10] S. Ha, Z. Dunbar, R.I. Masel, Characterization of a high performing passive direct formic acid fuel cell, J. Power Sources 158 (2006) 129–136.
[11] D. Morales-Acosta, J. Ledesma-Garcia, L.A. Godinez, H.G. Rodríguez, L. Álvarez-Contreras, L.G. Arriaga, Development of Pd and Pd–Co catalysts supported on multi-walled carbon nanotubes for formic acid oxidation, J.Power Sources. 195 (2010) 461–465.
[12] Z. Chen, D. Higgins, A. Yu, L. Zhang, J. Zhang, A review on non-precious metal electrocatalysts for PEM fuel cells, Energy Environ. Sci. 4 (2011) 3167–3192.
[13] M.G. Hosseini, M.M. Momeni, Evaluation of the Performance of Platinum Nanoparticle-Titanium Oxide Nanotubes as a New Refreshable Electrode for Formic Acid Electro-oxidation, Fuel Cells 12 (2012) 406–414.
[14] C. Nethravathi, E.A. Anumol, M. Rajamathi, N. Ravishankar, Highly dispersed ultrafine Pt and PtRu nanoparticles on graphene: formation mechanism and electrocatalytic activity, Nanoscale 3 (2011) 569–571.
[15] P. Hong, F. Luo, S. Liao, J. Zeng, Effects of Pt/C, Pd/C and PdPt/C anode catalysts on the performance and stability of air breathing direct formic acid fuel cells, Int. J. Hydrog. Energy. 36 (2011) 8518–8524.
[16] V. Mazumder, M. Chi, M.N. Mankin, Y. Liu, Ö. Metin, D. Sun, et al., A Facile Synthesis of MPd (M = Co, Cu) Nanoparticles and Their Catalysis for Formic Acid Oxidation, Nano Lett 12 (2012) 1102–1106.
[17] K. Ding, H. Jia, S. Wei, Z. Guo, Electrocatalysis of Sandwich-Structured Pd/Polypyrrole/Pd Composites toward Formic Acid Oxidation, Ind. Eng. Chem. Res. 50 (2011) 7077–7082.
[18] C. Xu, L. Cheng, P. Shen, Y. Liu, Methanol and ethanol electrooxidation on Pt and Pd supported on carbon microspheres in alkaline media, Electrochem. Commun. 9 (2007) 997–1001.
[19] Z.J. Mellinger, T.G. Kelly, J.G. Chen, Pd-Modified Tungsten Carbide for Methanol Electro-oxidation: From Surface Science Studies to Electrochemical Evaluation, ACS Catal. 2 (2012) 751–758.
[20] F. Hu, X. Cui, W. Chen, Ultralong-CNTA-Supported Pd-Based Anodes for Ethanol Oxidation, J. Phys. Chem. C 114 (2010) 20284–20289.
[21] Z. Bai, L. Yang, Y. Guo, Z. Zheng, C. Hu, P. Xu, High-efficiency palladiumcatalysts supported on ppy-modified C $_{60}$ for formic acid oxidation, Chem Commun. 47 (2011) 1752–1754.
[22] H. Huang, X. Wang, Pd nanoparticles supported on low-defect graphene sheets: for use as high-performance electrocatalysts for formic acid and methanol oxidation, J. Mater. Chem. 22 (2012) 22533–22541.
[23] K.-H. Ye, S.-A. Zhou, X.-C. Zhu, C.-W. Xu, P.K. Shen, Stability analysis of oxide (CeO2, NiO, Co3O4 and Mn3O4) effect on Pd/C for methanol oxidation in alkaline medium, Electrochim. Acta 90 (2013) 108–111.
[24] K. Ding, Y. Zhao, L. Liu, Y. Li, L. Liu, Y. Wang, et al., Multi-walled carbon nanotubes supported Pd composite nanoparticles hydrothermally produced from technical grade PdO precursor, Electrochim. Acta 176 (2015) 1256–1265.

[25] V.R. Khalap, T. Sheps, A.A. Kane, P.G. Collins, Hydrogen Sensing and Sensitivity of Palladium-Decorated Single-Walled Carbon Nanotubes with Defects, Nano Lett 10 (2010) 896–901.
[26] M. Zhang, Z. Yan, J. Xie, Core/shell Ni@Pd nanoparticles supported on MWCNTs at improved electrocatalytic performance for alcohol oxidation in alkaline media, Electrochim. Acta 77 (2012) 237–243.
[27] M.D. Sánchez, P. Chen, T. Reinecke, M. Muhler, The Role of Oxygen- and Nitrogen-containing Surface Groups on the Sintering of Iron Nanoparticles on Carbon Nanotubes in Different Atmospheres, ChemCatChem 4 (2012) 1997–2004.
[28] M. Park, B.-H. Kim, S. Han, D.-S. Han, G. Kim, K.-R. Lee, Improved binding between copper and carbon nanotubes in a composite using oxygen-containing functional groups, Carbon 49 (2011) 811–818.
[29] J.-Y. Wang, H.-X. Zhang, K. Jiang, W.-B. Cai, From HCOOH to CO at Pd Electrodes: A Surface-Enhanced Infrared Spectroscopy Study, J. Am. Chem. Soc. 133 (2011) 14876–14879.
[30] J. Xu, D. Yuan, F. Yang, D. Mei, Z. Zhang, Y.-X. Chen, On the mechanism of the direct pathway for formic acid oxidation at a Pt(111) electrode, Phys. Chem. Chem. Phys. 15 (2013) 4367–4376.
[31] M. Ren, Y. Kang, W. He, Z. Zou, X. Xue, D.L. Akins, et al., Origin of performance degradation of palladium-based direct formic acid fuel cells, Appl. Catal. B Environ. 104 (2011) 49–53.
[32] W. Zhou, J. Xu, Y. Du, P. Yang, Polycarbazole as an efficient promoter for electrocatalytic oxidation of formic acid on Pt and Pt–Ru nanoparticles, Int. J. Hydrog. Energy. 36 (2011) 1903–1912.
[33] W. Gao, J.A. Keith, J. Anton, T. Jacob, Theoretical Elucidation of the Competitive Electro-oxidation Mechanisms of Formic Acid on Pt(111), J. Am. Chem. Soc. 132 (2010) 18377–18385.
[34] J.V. Perales-Rondón, E. Herrero, J.M. Feliu, Effects of the anion adsorption and pH on the formic acid oxidation reaction on Pt(111) electrodes, Electrochim. Acta 140 (2014) 511–517.
[35] Y. Kim, H.J. Kim, Y.S. Kim, S.M. Choi, M.H. Seo, W.B. Kim, Shape- and Composition-Sensitive Activity of Pt and PtAu Catalysts for Formic Acid Electrooxidation, J. Phys. Chem. C 116 (2012) 18093–18100.
[36] M.E. Scofield, C. Koenigsmann, L. Wang, H. Liu, S.S. Wong, Tailoring the composition of ultrathin, ternary alloy PtRuFe nanowires for the methanol oxidation reaction and formic acid oxidation reaction, Energy Env. Sci. 8 (2015) 350–363.
[37] M. Shao, J. Odell, M. Humbert, T. Yu, Y. Xia, Electrocatalysis on Shape-Controlled Palladium Nanocrystals: Oxygen Reduction Reaction and Formic Acid Oxidation, J. Phys. Chem. C 117 (2013) 4172–4180.
[38] H. Li, G. Sun, Q. Jiang, M. Zhu, S. Sun, Q. Xin, Synthesis of highly dispersed Pd/C electro-catalyst with high activity for formic acid oxidation, Electrochem. Commun. 9 (2007) 1410–1415.
[39] X. Yu, P.G. Pickup, Mechanistic study of the deactivation of carbon supported Pd during formic acid oxidation, Electrochem. Commun. 11 (2009) 2012–2014.
[40] J.D. Lović, A.V. Tripković, S.L. Gojković, K.D. Popović, D.V. Tripković, P. Olszewski, et al., Kinetic study of formic acid oxidation on carbon-supported platinum electrocatalyst, J. Electroanal. Chem. 581 (2005) 294–302.
[41] J. Joo, T. Uchida, A. Cuesta, M.T.M. Koper, M. Osawa, The effect of pH on the electrocatalytic oxidation of formic acid/formate on platinum: A mechanistic study by surface-enhanced infrared spectroscopy coupled with cyclic voltammetry, Electrochim. Acta 129 (2014) 127–136.
[42] Y. Wang, Q. He, J. Guo, H. Wei, K. Ding, H. Lin, et al., Carboxyl Multiwalled Carbon-Nanotube-Stabilized Palladium Nanocatalysts toward Improved Methanol Oxidation Reaction, ChemElectroChem 2 (2015) 559–570.
[43] T. Das, S. Banerjee, K. Dasgupta, J.B. Joshi, V. Sudarsan, Nature of the Pd–CNT interaction in Pd nanoparticles dispersed on multi-walled carbon nanotubes and its implications in hydrogen storage properties, RSC Adv. 5 (2015) 41468–41474.
[44] Y. Wang, Q. He, H. Qu, X. Zhang, J. Guo, J. Zhu, et al., Magnetic graphene oxide nanocomposites: nanoparticles growth mechanism and property analysis, J Mater Chem C 2 (2014) 9478–9488.
[45] S. Piscanec, M. Lazzeri, J. Robertson, A.C. Ferrari, F. Mauri, Optical phonons in carbon nanotubes: Kohn anomalies, Peierls distortions, and dynamic effects, Phys. Rev. B 75 (2007) .
[46] Y. Wang, Q. He, K. Ding, H. Wei, J. Guo, Q. Wang, et al., Multiwalled Carbon Nanotubes Composited with Palladium Nanocatalysts for Highly Efficient Ethanol Oxidation, J. Electrochem. Soc. 162 (2015) F755–F763.
[47] N. Hoshi, K. Kida, M. Nakamura, M. Nakada, K. Osada, Structural Effects of Electrochemical Oxidation of Formic Acid on Single Crystal Electrodes of Palladium, J. Phys. Chem. B 110 (2006) 12480–12484.
[48] U. Schlotterbeck, C. Aymonier, R. Thomann, H. Hofmeister, M. Tromp, W. Richtering, et al., Shape-Selective Synthesis of Palladium Nanoparticles Stabilized by Highly Branched Amphiphilic Polymers, Adv. Funct. Mater. 14 (2004) 999–1004.
[49] P. Kannan, T. Maiyalagan, M. Opallo, One-pot synthesis of chain-like palladium nanocubes and their enhanced electrocatalytic activity for fuel-cell applications, Nano Energy 2 (2013) 677–687.
[50] R.K. Pandey, V. Lakshminarayanan, Enhanced Electrocatalytic Activity of Pd-Dispersed 3,4-Polyethylenedioxythiophene Film in Hydrogen Evolution and Ethanol Electro-oxidation Reactions, J. Phys. Chem. C 114 (2010) 8507–8514.
[51] Y. Zhou, J. Liu, J. Ye, Z. Zou, J. Ye, J. Gu, et al., Poisoning and regeneration of Pd catalyst in direct formic acid fuel cell, Electrochim. Acta 55 (2010) 5024–5027.
[52] T. Jin, S. Guo, J. Zuo, S. Sun, Synthesis and assembly of Pd nanoparticles on graphene for enhanced electrooxidation of formic acid, Nanoscale 5 (2013) 160–163.
[53] J. Yang, C. Tian, L. Wang, H. Fu, An effective strategy for small-sized and highly-dispersed palladium nanoparticles supported on graphene with excellent performance for formic acid oxidation, J. Mater. Chem. 21 (2011) 3384–3390.
[54] D.W. Yuan, Z.R. Liu, Atomic ensemble effects on formic acid oxidation on PdAu electrode studied by first-principles calculations, J. Power Sources 224 (2013) 241–249.
[55] Z. Liu, L. Hong, M.P. Tham, T.H. Lim, H. Jiang, Nanostructured Pt/C and Pd/C catalysts for direct formic acid fuel cells, J. Power Sources 161 (2006) 831–835.
[56] W. Chen, J. Kim, S. Sun, S. Chen, Electro-oxidation of formic acid catalyzed by FePt nanoparticles, Phys. Chem. Chem. Phys. 8 (2006) 2779–2786.
[57] W. Chen, J. Kim, S. Sun, S. Chen, Composition Effects of FePt Alloy Nanoparticles on the Electro-Oxidation of Formic Acid, Langmuir 23 (2007) 11303–11310.
[58] J. Chang, L. Feng, C. Liu, W. Xing, X. Hu, Ni2P enhances the activity and durability of the Pt anode catalyst in direct methanol fuel cells, Energy Environ. Sci. 7 (2014) 1628–1632.
[59] Y. Lu, W. Chen, Nanoneedle-Covered Pd-Ag Nanotubes: High Electrocatalytic Activity for Formic Acid Oxidation, J. Phys. Chem. C. 114 (2010) 21190–21200.
[60] W. Chen, S. Chen, Iridium-platinum alloy nanoparticles: Composition-dependent electrocatalytic activity for formic acid oxidation, J. Mater. Chem. 21 (2011) 9169–9178.
[61] M. Arenz, V. Stamenkovic, T.J. Schmidt, K. Wandelt, P.N. Ross, N.M. Markovic, The electro-oxidation of formic acid on Pt-Pd single crystal bimetallic surfaces, Phys. Chem. Chem. Phys. 5 (2003) 4242–4251.
[62] A.V. Tripković, S.L. Gojković, K.D. Popović, J.D. Lović, A. Kowal, Study of the kinetics and the influence of Biirr on formic acid oxidation at Pt2Ru3/C, Electrochim. Acta 53 (2007) 887–893.
[63] Y. Wang, B. Wu, Y. Gao, Y. Tang, W. Lu, W. Xing, et al., Kinetic study of formic acid oxidation on carbon supported Pd electrocatalyst, J. Power Sources 192 (2009) 372–375.
[64] H. Wang, L. Thia, N. Li, X. Ge, Z. Liu, X. Wang, Selective electro-oxidation of glycerol over Au supported on extended poly(4-vinylpyridine) functionalized graphene, Appl. Catal. B Environ. 166–167 (2015) 25–31.